

Electrochemical Instability of Metal–Organic Frameworks: In Situ Spectroelectrochemical Investigation of the Real Active Sites

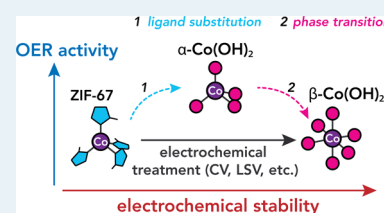
Weiran Zheng,¹ Mengjie Liu, and Lawrence Yoon Suk Lee^{1*}

Department of Applied Biology and Chemical Technology and The State Key Laboratory of Chemical Biology and Drug Discovery, The Hong Kong Polytechnic University, Hung Hom, Kowloon, Hong Kong SAR, China

Supporting Information

ABSTRACT: Despite recent attempts using metal–organic frameworks (MOFs) directly as electrocatalysts, the electrochemical stability of MOFs and the role of in situ-formed species during electrochemistry are elusive. Using in situ spectroelectrochemistry, we present herein a comprehensive discussion on the structural and morphological evolution of MOFs (zeolitic imidazolate framework-67, ZIF-67) during both cyclic voltammetry and amperometry. Dramatic morphological changes exposing electron-accessible Co sites are evident. The intense conversion from tetrahedral Co sites in ZIF-67 to tetrahedral α -Co(OH)₂ and octahedral β -Co(OH)₂, and the formation of their corresponding oxidized forms (CoOOH), is observed during both the electrochemical treatments. Subsequent oxygen evolution reaction suggests the CoOOH produced from α/β -Co(OH)₂ as the dominating active sites, not the metal nodes of ZIF-67. Specifically, the CoOOH from α -Co(OH)₂ is most active (turnover frequency = 0.59 s⁻¹) compared to that from β -Co(OH)₂ (0.06 s⁻¹). Our study demonstrates the importance of examining the electrochemical stability of MOFs for electrocatalyst design.

KEYWORDS: ZIF-67, in situ UV–vis, in situ Raman, spectroelectrochemistry, electrochemical stability, cobalt hydroxide, oxygen evolution reaction



1. INTRODUCTION

Metal–organic frameworks (MOFs), composed of metal ions or clusters coordinated with organic linker molecules, have received a spotlight in material research since the last decade because of their structural flexibility.¹ Currently, a number of tailor-designed MOFs have demonstrated high efficiencies in both energy and environmental applications, such as gas storage, separation, sensing, energy storage, and conversion.^{2,3} Especially, for the holy grail of energy-related electrocatalysis, such as CO₂ reduction and water splitting, the unique characteristics of MOFs have made them good candidates.^{4,5} On the one hand, the permanent porosity of MOFs can facilitate the rapid mass transfer of substrates and products throughout the bulk material, unleashing the limitation that restricts the reaction rate of many conventional electrocatalysts.⁶ On the other hand, the well-defined single metal sites are analogous to the molecular catalysts, enabling MOFs to act as single-atom electrocatalysts with 100% atom utilization.⁷ Moreover, the electronic properties of metal sites can be tuned by altering the linker, adding further flexibility of catalyst design toward the desired performance. Based on such guidelines, various MOF-based electrocatalysts have been designed to achieve superior performances in electrocatalysis.⁸ Especially, because of the importance of the oxygen evolution reaction (OER) in water splitting, Co-MOFs,^{9,10} NiCo-MOFs,^{11–13} FeCo-MOFs,^{14,15} and NiFe-MOFs^{16,17} have been extensively explored, and all of them imply the atomic metal nodes as the real active sites for oxygen production.

However, attributing electrocatalytic activity exclusively to metal nodes is valid only if the MOF structure remains intact throughout the electrochemical processes. As recently suggested by many researchers, the in situ conversion of the pristine electrocatalysts during the OER is critical for their high performance, and the intermediates are identified as the real active sites.¹⁸ Taking Co-based electrocatalysts as an example, recent operando evidence suggests the conversion of Co²⁺ (Co(OH)₂ and CoO_x) to Co³⁺ (CoOOH) as a precatalytic electrochemical process, and both oxidized forms of Co²⁺, including Co³⁺ and Co⁴⁺, are assigned for OER activity.^{19,20} In such cases, the pristine electrocatalysts act as the precatalysts for active site production. A similar phenomenon is also likely for MOFs because the mechanism of OER requires the formation of M–OH⁻ and electrooxidation to M–OOH (M = metal),¹⁹ indicating the replacement of coordinating linker molecules by hydroxide ions. Considering that the metal–linker coordination is the backbone of MOFs, such replacements can result in partial or major structural destruction. However, despite multiple reports suggesting the formation of metal oxides in the MOFs after (during) electrocatalysis,^{17,21} the information on the electrochemical evolution of MOFs and the role of the formed structures are not available yet. Also, the coexisting in situ-generated metal species during electrochemical treatments [e.g., cyclic voltammetry (CV) and

Received: September 4, 2019

Revised: October 29, 2019

Published: November 21, 2019

amperometry] further complicates the understanding of the real active sites.

Consequently, the interpretation of the OER activity based on ex situ characterizations before the electrocatalysis could be, sometimes, misleading. For example, both NiO and Fe₂O₃ polycrystalline structures are formed after the OER process using NiFe-MOFs,¹⁷ and the assignment of real active sites can be difficult because both NiO and Ni/Fe nodes can provide the sites for M–OOH formation. Furthermore, such coexistence of active species can obscure the interpretation of CV and amperometry because of the mixed redox signals arising from metal nodes and intermediates, especially when many researchers prefer to present only the “stable” cycle of plots.

One strategy to address such dispute is the in situ techniques coupled with electrochemistry, as demonstrated previously on other electrocatalysts. For example, Koel et al. used in situ Raman spectroscopy to identify the formation of NiOOH as the reason for improved OER activity in the NiCoO_xH_y material.¹⁸ Using operando ambient pressure X-ray photoelectron spectroscopy (XPS), Favaro et al. revealed the complete conversion of Co(OH)₂ to CoOOH before OER potential and the production of Co⁴⁺ during OER.²⁰ However, neither the in situ electrochemical studies of MOFs during electrochemical treatments nor the role of in situ-formed species during the precatalytic electrochemical processes, as the fundamental aspect of MOF-based electrocatalysts, is available yet.

Herein, we present the first comprehensive discussion on the morphological and structural evolution of MOFs during two typical electrochemical treatments: CV and amperometry. Zeolitic imidazolate framework-67 (ZIF-67), one of the most widely used MOFs and relatively stable in an aqueous solvent, is studied as a representative demonstration. Evidence from both in situ UV–vis spectra and in situ Raman spectra, as well as ex situ characterizations such as electron microscopy, powder diffraction, and XPS, is discussed to unveil the full image of the evolution of ZIF-67. Finally, the role of the in situ-formed species during precatalytic and catalytic processes is revealed as the dominating active sites of ZIF-67 responsible for its enhanced OER activity.

2. RESULTS AND DISCUSSION

2.1. Morphology of ZIF-67. Figure 1A shows a representative structural unit of pristine ZIF-67 hosting a pore of ca. 1.70 nm constructed by tetrahedral Co sites coordinated with four 2-methylimidazole (mIM) molecules (denoted as Co(mIM)₄). As the platform material, cubic ZIF-67 is obtained following an established method²² with a mean edge length of 158 nm (Figure 1B). The ZIF-67-modified carbon fiber paper (ZIF-67@CFP) electrode shows evenly coated ZIF-67 nanocubes on the carbon fiber surface (Figure 1C). MOFs are known as electron beam-sensitive crystalline materials, and their high-resolution imaging is still challenging to date.²³ The transmission electron microscopy (TEM) image (Figure 1D) and the high-resolution images of selected regions (Figure 1E–G showing the center, corner, and edge regions) show no clear crystalline structure of ZIF-67, also indicated by the featureless selected area electron diffraction (SAED) patterns, such results rule out the other Co-based structures. It is worth to note that no significant electron beam damage is observed during the imaging of pristine ZIF-67 at 200 kV even with a relatively long imaging time (6 min), nor any other

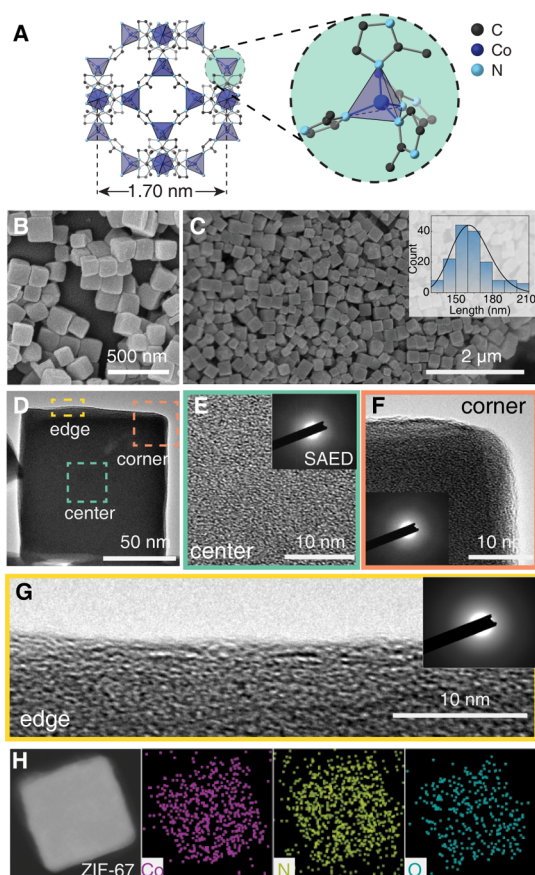


Figure 1. Morphology of ZIF-67@CFP electrode. (A) Representative structural unit of pristine ZIF-67 showing the tetrahedral Co site. SEM images of (B) ZIF-67 nanocubes and (C) surface of the ZIF-67@CFP electrode. The inset shows the size distribution. TEM images of (D) a single ZIF-67 nanocube and its (E) center, (F) corner, and (G) edge regions. The inset shows the SAED patterns of the selected region. (H) Dark-field TEM images of a nanocube and its corresponding Co, N, and O elemental mappings.

crystalline structures (Movie S1). Elemental mappings on a dark-field TEM image (Figure 1H) suggest uniformly distributed Co, N, and O, and the presence of O is attributed to the physisorbed H₂O and OH[−].

2.2. CV Precatalytic Treatment. CV is one of the most popular and fundamental techniques to study the electrochemical properties of materials. During a typical CV study, a cycling external potential is applied on the surface of the modified electrode, promoting the formation of an electrochemical double layer and/or electron exchanges between the electrode and electrolyte. Various reactions, including chemical and redox processes, occur during CV treatment depending on the applied potential. Needless to say, the reliability of CV profiles is based on the presupposition that modified electrodes are stable during CV treatment.

Therefore, to verify the presupposition, we performed CV treatment in 1.0 M KOH electrolyte for 100 cycles using the ZIF-67@CFP electrode. Moreover, CV of ZIF-67 is studied within three potential windows [0.925–1.025 V (denoted as 0.1), 0.925–1.325 V (denoted as 0.4), and 0.925–1.525 V (denoted as 0.6) vs reversible hydrogen electrode] to separate different electrochemical processes accompanying the potential change.

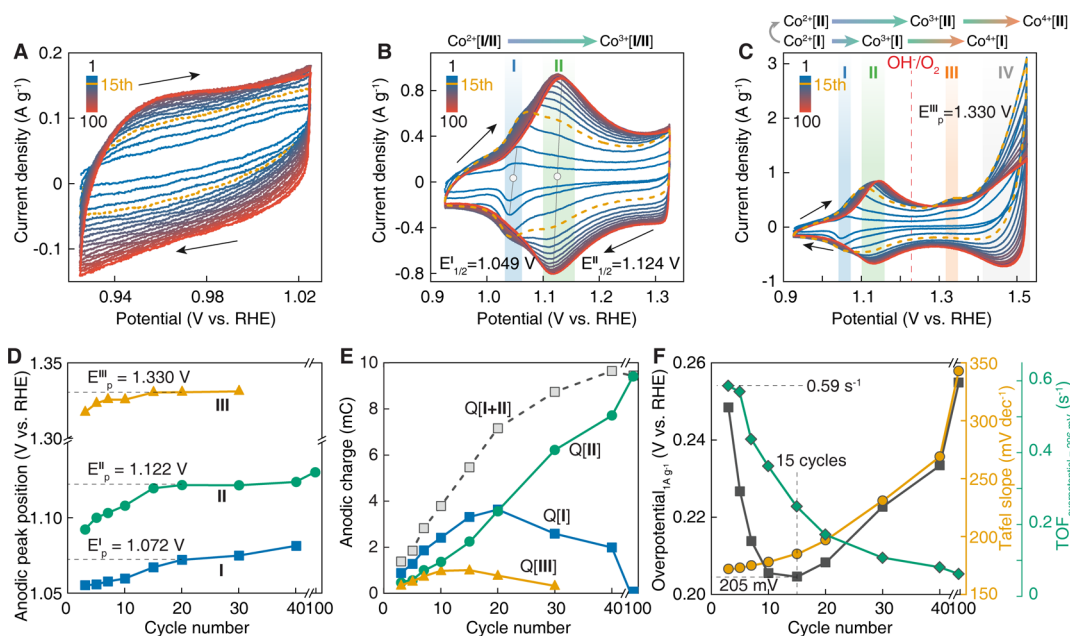


Figure 2. CV study of ZIF-67@CFP electrode. Continuous cyclic voltammograms (1, 5, 10, ..., 100) of the ZIF-67@CFP electrode in 1.0 M KOH electrolyte between (A) 0.925 and 1.025 V, (B) 0.925 and 1.325 V, and (C) 0.925 and 1.525 V. The scan rate is 10 mV s⁻¹. The 15th scan is highlighted as yellow dotted lines. Plots showing the change of (D) anodic peak position, (E) anodic charge, and (F) OER overpotential (current density = 1 A g⁻¹), Tafel slope, and TOF (overpotential = 296 mV) with cycle number.

Within 0.1, the ZIF-67@CFP electrode shows a typical capacitor behavior (Figure 2A), where the non-Faradaic charge/discharge currents increase from the 1st to 60th cycles and stabilize thereafter. Considering that the current mainly arises from the adsorption and release of hydroxide ions within the double-layer region for capacitors, the increasing trend of the current suggests the growth of the electrochemical surface area (ECSA) of ZIF-67 with cycle numbers. Moreover, the kinetic aspects of the OH⁻ ion diffusion can be revealed by electrochemical impedance spectroscopy (EIS). For a stable porous material, the phase angle of the straight line in the mid-frequency region is mainly controlled by the material morphology and the surface area,²⁴ and the large-phase angle value indicates fast ion diffusion. Figure S1A shows the Nyquist plots of the ZIF-67@CFP electrode cycled within 0.1. Before cycling, the phase angle is larger than 45° in the mid-frequency region deviating from the Warburg diffusion element, representing a high OH⁻ diffusion rate possibly because of the porous trait of MOFs and the rapid coordination between the OH⁻ and Co sites in the pores. During CV cycling, the phase angle decreases first (0–30 cycle) and increases back slightly (30–100 cycle). Such a trend indicates the same change in the OH⁻ diffusion behavior. The initial drop can be related to the morphological evolution of ZIF-67 (possible loss of pore of ca. 1.70 nm), while the following increment to the establishment of new microstructures with better OH⁻ adsorption/desorption capability. However, because the molecule structure of ZIF-67 could be unstable during the CV study, the detailed reason behind the kinetic trend of ion diffusion can be more complicated.

At a wider potential window of 0.4 (Figure 2B), apart from the increasing ECSA, two recognizable redox couples (marked as regions I and II) with half-wave potentials ($E_{1/2}$) at 1.049 and 1.124 V evolve until the 40th cycle. Both can be attributed to the redox between Co²⁺ and Co³⁺ species, yet the different $E_{1/2}$ values indicate the existence of two Co²⁺ species (we

denote them as Co²⁺[I] and Co²⁺[II] temporarily here to avoid confusion, until they are confirmed as α - and β -Co(OH)₂, respectively, in Section 2.4). Moreover, the increasing anodic peak current suggests the continuous exposure of more accessible Co sites. After 40 cycles, only the redox couple at 1.124 V remains with the plateaued anodic peak current, indicating that the MOF structure is converted to a CV-stable structure. Notably, incomplete reduction of Co³⁺ species is suggested by the larger anodic peak current than the cathodic one (e.g., at the 40th cycle, anodic: 0.537 A g⁻¹; cathodic: 0.411 A g⁻¹). The phase angle first decreases until the 15th cycle and slightly increases from the 16th to 100th cycles (Figure S1B). The initial decline marks the porosity loss of MOFs, while the subsequent rise could be reasoned by the production of a Co-based microstructure after CV precatalytic treatment. A new anodic peak (peak potential E_p = 1.330 V, marked as region III) appears after cycling within 0.6 (Figure 2C), indicating the electrooxidation of Co³⁺ to Co⁴⁺ species. Unlike regions I and II, region III shows no corresponding cathodic peak, mainly because the unstable Co⁴⁺ species can rapidly undergo a coupled chemical reduction to Co³⁺.¹⁹ Apart from the precatalytic I, II, and III regions, the catalytic OER occurs at a higher potential (region IV) and reaches the maximum current between the 15th and 20th cycles. Similar to the CV treatment within 0.4 but in a swifter fashion (phase angle drops and rises in fewer cycle numbers), the phase angle (Figure S1C) declines until the 5th cycle and rises between the 6th and 10th cycles, while further cycles bring negligible changes. The 100th cycle shows a higher phase angle of 76° compared to 65°. Therefore, the CV precatalytic treatment at a wider potential range, that is, 0.6, not only causes the quick destruction of MOF porosity but also the fast production of a new porous Co-based structure.

By deconvoluting the CV plots (example shown in Figure S2), both peak position and charge of the three anodic peaks in regions I, II, and III can be quantitated. As potential cycling

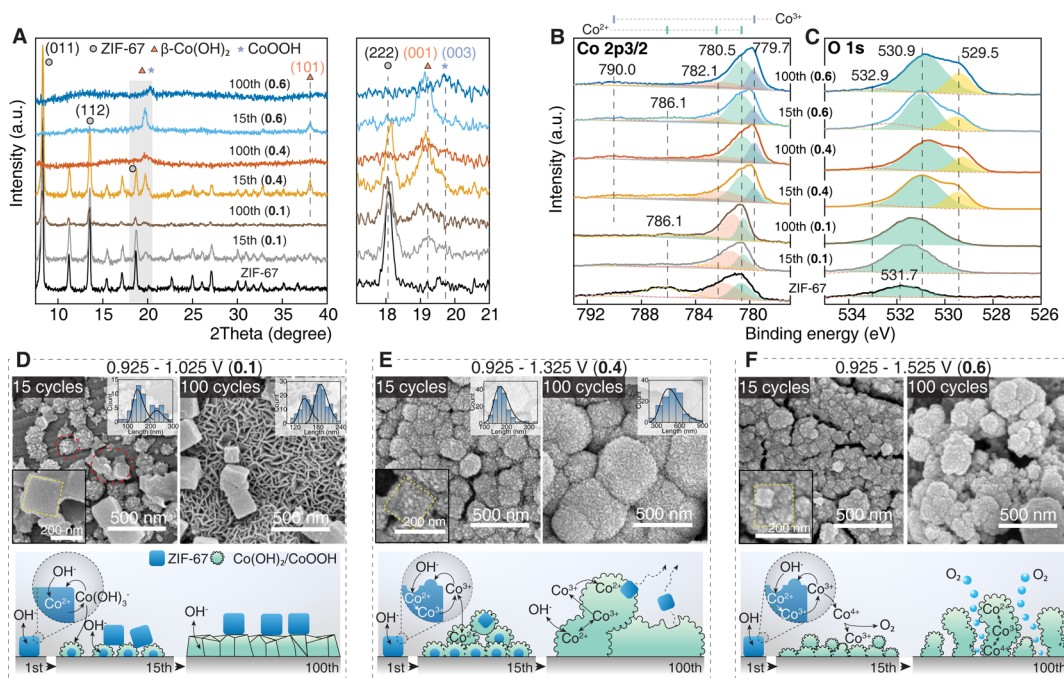


Figure 3. Structure and morphology of ZIF-67@CFP electrode after CV treatment. (A) XRD patterns of pristine and CV-treated ZIF-67 with different cycles (15 and 100) between different potential ranges: **0.1** (0.925–1.025 V), **0.4** (0.925–1.325 V), and **0.6** (0.925–1.525 V). The zoom-in view emphasizes ZIF-67 (222), β -Co(OH)₂ (001), and CoOOH (003). XPS spectra of (B) Co 2p_{3/2} and (C) O 1s region of pristine and CV-treated ZIF-67 with different cycles (15 and 100) between different potential ranges: **0.1**, **0.4**, and **0.6**. SEM images of ZIF-67 after CV treatment and the corresponding illustration of structural evolution between (D) **0.1**, (E) **0.4**, and (F) **0.6** for 15 and 100 cycles. The insets show the zoom-in view and size distribution.

proceeds (Figure 2D), all peaks shift to higher potential values until the 20th cycle and stabilize at 1.072, 1.122, and 1.330 V, respectively. Such peak shifting could be understood by the collective effect of larger ECSA (thus increased number of Co²⁺ species) and the structural evolution of Co²⁺ to its stable form (thus higher oxidation potential). The anodic charges shown as Q[I] and Q[II] for anodic peaks I and II in Figure 2E denote the numbers of electron-accessible Co²⁺ sites. The uprising trend of Q[I] observed in the first 20 cycles implies the increasing concentration of Co²⁺[I] species, while further cycles decrease its total number. Q[II], however, continues to increase with cycle numbers throughout the entire CV studies. The increment between the 1st and 20th cycles indicates that both Co²⁺ species are exposed as a result of CV treatment, yet the declining trend of Q[I] shows that Co²⁺[I] is unstable during CV and can be converted, possibly, to Co²⁺[II]. Q[I + II], representing the total amount of electrochemically accessible Co²⁺ species, shows an increasing trend between the 1st and 40th cycles, rendering the continuous exposure of Co²⁺ species. After 40 cycles, the total anodic charge reaches 9.80 mC (1.02 × 10⁻⁴ mmol of Co²⁺), which is merely 1.3% of the total Co²⁺ (7.92 × 10⁻³ mmol) on the electrode. Because the oxidation of Co²⁺ to Co³⁺ requires both electrons and OH⁻, such a low percentage shows that only the surface Co²⁺ species can be accessed by electrons and OH⁻, during the CV treatment. Further cycling to 100 cycles results in the negligible changes to 9.45 mC, an indication of established ECSA and stable surface Co²⁺ species. The Co³⁺ to Co⁴⁺ electrooxidation charge, denoted as Q[III], follows a similar trend as Q[I], reaching the maximum at the 15th cycle and completely disappearing after 30 cycles. Such a correlation between Q[I] and Q[III] indicates that they are related to the continuous electrooxidation of the same Co²⁺ species:

$$\text{Co}^{2+}[\text{I}] \xrightarrow{Q[\text{I}]} \text{Co}^{3+}[\text{I}] \xrightarrow{Q[\text{III}]} \text{Co}^{4+}[\text{I}].$$

The Co³⁺[II] to Co⁴⁺[II] electrooxidation signal is overlapping with the OER catalytic current; thus, it is not differentiable. Therefore, instead of acting as an electrocatalyst, ZIF-67 is more like a precatalyst, and the precatalytic CV process can produce two electron-accessible Co²⁺ species with different Co²⁺–Co³⁺–Co⁴⁺ oxidation potentials.

The impact of precatalytically produced species on the catalytic OER process is presented in Figure 2F, where the change in OER properties is given in correlation with the CV cycle number. Because the precatalytic conversion of Co²⁺ to Co³⁺ and Co⁴⁺ is electrochemically inevitable and both Co³⁺ and Co⁴⁺ are considered as the real active sites,²⁰ we use Co[I] and Co[II] in the following context to represent the oxidized forms of Co²⁺[I] and Co²⁺[II] for clarification. The declining trend of turnover frequency (TOF) at an overpotential of 296 mV shows that the normalized activity of Co sites decreases from 0.59 s⁻¹ (after 3 cycles) to 0.06 s⁻¹ (after 100 cycles) with a 90% activity loss. The continuous transformation from more active Co[I] to less active Co[II] species is thus suggested, leading to the collective activity drop of Co sites. Notably, the TOF value at the third cycle is six times higher than the previously reported Co chalcogenide.²⁵ Also, the Tafel slope (Tafel plot shown in Figure S3) increases with the cycle number, showing a decreasing OER kinetic rate after more CV stripping. The lowest overpotential for a current density of 1 A g⁻¹ is 205 mV after 15 cycles. The inversed volcano-type trend of overpotential is jointly decided by the total number of active sites and the activity of a particular site: at lower cycle numbers, only limited concentration of Co²⁺ species as the precatalyst is available for OER; at higher cycle

numbers, active Co[I] sites are completely converted to relatively inactive Co[II] sites.

2.3. Structural and Morphological Evolution of ZIF-67 during CV Precatalytic Treatment. As shown in Figure 3A, the ex situ X-ray powder diffraction (XRD) pattern of pristine ZIF-67 matches well with the previous report,²⁶ where two intensive peaks at 7.4 and 12.8° are assigned to (011) and (112) facets, respectively. The pattern of ZIF-67 is retained after both 15 and 100 cycles between 0.925 and 1.025 V (0.1). The broadening of (011) peak, however, indicates that the crystallite size is decreased. A minor peak appears at 19.2° after 15 cycles, representing the (001) plane of β -Co(OH)₂ (JCPDS 30-0443).²⁷ At a wider window of 0.4, besides the β -Co(OH)₂, verified by its (001) and (101) facets at 19.2 and 38.1°, respectively, the electrooxidation of Co²⁺ to Co³⁺ starts, as confirmed by the distinct formation of CoOOH (shoulder peak at 19.7° attributed to its (003) plane (JCPDS 78-11213)).²⁷ The ZIF-67 peaks have vanished after 100 cycles. Further expansion of potential window to 0.6 leads to the complete devastation of ZIF-67 after only 15 cycles. The dominating β -Co(OH)₂ after 15 cycles have changed to CoOOH after 100 cycles as indicated by the single peak at 19.7°. Therefore, the ZIF-67 structure is unstable during CV treatments, eventually converted to β -Co(OH)₂ and CoOOH, depending on the CV potential windows.

The presence of Co, N, and O species on the surface of the electrode before and after CV precatalytic treatment was confirmed by the XPS (Figure S4A). The pristine ZIF-67 shows a surface N-to-Co atomic ratio of 3.63, slightly lower than the stoichiometric number of 4. It is likely that a portion of surficial Co coordination sites is occupied by the physisorbed H₂O. As shown in Table S1, the CV precatalytic treatments lead to the dramatic decrement of N-to-Co ratio to 0.77 (15 cycles within 0.1), 0.62 (15 cycles within 0.4), 0.69 (15 cycles within 0.6), and eventually to 0.39 (0.1) and 0.21 (0.4 and 0.6) after 100 cycles, revealing the destruction of ZIF-67. Meanwhile, the rapid drop of surface N-to-O ratio from 4.81 to 0.13 (0.1) and 0.08 (0.4 and 0.6) after 100 cycles confirms the replacement of surface coordinating N-containing linker molecules (loss to electrolyte during CV) by OH⁻/O²⁻ after the precatalytic electrochemical process. Such a replacement is also suggested by the reduced N 1s peak after CV treatment (Figure S4B).

Examining the Co 2p_{3/2} peak of pristine ZIF-67 (Figure 3B) reveals three peaks at 780.5, 782.1, and 786.1 eV. The former two peaks are ascribed to the surface Co species coordinated with OH⁻ and mIM linkers and the last to the satellite peak. The distances between the satellite peak and the main peaks are 5.6 and 4.0 eV, indicating that all Co species of ZIF-67 is in the form of Co²⁺.^{28,29} Within 0.1, no significant evolution of the Co²⁺ signal is observed after 15 and 100 cycles, showing no valence changes. After the CV treatment involving the redox between Co²⁺–Co³⁺ (0.4) and Co²⁺–Co³⁺–Co⁴⁺ (0.6), a new peak at 779.7 eV, assigned to the Co³⁺ species, evolves from all samples, as well as another satellite peak at 790.0 eV. The distance between the two new peaks is 10.3 eV, confirming the existence of Co³⁺ species,³⁰ which is in good agreement with the XRD results of finding CoOOH (Figure 3A). Meanwhile, both physisorbed H₂O (532.9 eV) and OH⁻ (531.7 eV) exist on the surface of pristine ZIF-67 (Figure 3C). A single peak of OH⁻ is observed after cycling within 0.1, which shifts slightly from 531.5 eV (15 cycles) to 531.1 eV (100 cycles). Such a peak shifting can be reasoned by the gradual structural

transition from Co–OH within the ZIF-67 coordination environment to crystalline Co(OH)₂.

After cycling within higher potential windows (0.4 and 0.6), the oxide ions (O²⁻) from CoOOH is evident by the peak at 529.5 eV,³⁰ accompanied by the shifting of OH⁻ peak to 530.9 eV. Such shifting indicates the different coordination environments of OH⁻ species on tetrahedral ZIF-67 (the initial structure) and octahedral β -Co(OH)₂ (the final structure). Notably, despite the finding of OH⁻ in ZIF-67 structure by XPS, no Co(OH)₂ structure is suggested by the XRD result, indicating that only neglectable mIM linkers are replaced by OH⁻ while the Co coordination configuration of ZIF-67 remains in the pristine state. Because the first cycle of ZIF-67 shows mainly a Co²⁺[I] oxidation signal (Figure 2B), we believe that the OH⁻ signal observed from XPS originates from the minor Co²⁺[I].

Dramatic morphological changes induced by CV are shown by the scanning electron microscopy (SEM) images in Figure 3D–F (zoom-out images of a single CFP shown in Figure S5). With only the capacitive process involved within 0.1, the deformation of ZIF-67 nanocubes is observed after 15 cycles, forming smaller island-like nanoparticles (ca. 145 nm mean diameter), which further transforms into vertically aligned nanosheets at the 100th cycle. The nanosheets have β -Co(OH)₂ structure as indicated by previous XRD results, and a similar morphology was also reported from the electrodeposited β -Co(OH)₂.³¹ The transition process is illustrated in Figure 3D, where hydroxide ions travel into the porous ZIF-67 structure during the anodic scan (charge process) and replace the mIM linker to form Co(OH)₃⁻ ions. The reverse cathodic scan forces Co(OH)₃⁻ out of the framework (discharge process), destroying the ZIF-67 structure. Another anodic scan attracts Co(OH)₃⁻ on the surface of carbon fiber to form a Co(OH)₂ structure, similar to the electrodeposition process. The formation of such a nanosheet structure with high ECSA also explains the increased capacitance in Figure 2A. Surprisingly, some of the nanocubes persist after 100 cycles, presumably because only the ZIF-67 nanocubes in direct contact with CFP can be accessed by electron and potential and are thus subject to the potential-driven OH⁻ sorption and Co(OH)₃⁻ desorption. When the Co²⁺–Co³⁺ redox processes are involved (within 0.4), the final β -Co(OH)₂ structure tends to adopt a spherical shape with a mean diameter of 164 nm at the 15th cycle, which grows to 477 nm after 100 cycles. The deformed nanocubes act as nucleation sites on which the produced CoOOH can be reduced. The cubic vacancies observed in Figure S6 support such an explanation. As the potential window reaches 0.6, the oxidation of Co³⁺ to Co⁴⁺ actuates, followed by O₂ discharge. The cracks formed after 15 cycles and pores after 100 cycles are due to the evolution of O₂ from Co sites. Such morphology makes it practically impossible to analyze the particle size.

Therefore, as proved by the ex situ characterization after CV studies, ZIF-67 is converted to β -Co(OH)₂ and CoOOH structure as the final form, depending on the potential windows. However, the intermediated species between such conversion needs to be revealed by in situ studies.

2.4. In Situ Spectroelectrochemistry of the First CV Cycle. To understand the precatalytic transition of Co sites with tetrahedral coordination in ZIF-67 to octahedral in β -Co(OH)₂ and the assignment of Co²⁺[I] and Co²⁺[II], in situ spectroelectrochemical methods, including in situ UV–vis and Raman spectroscopy, are employed to investigate the first

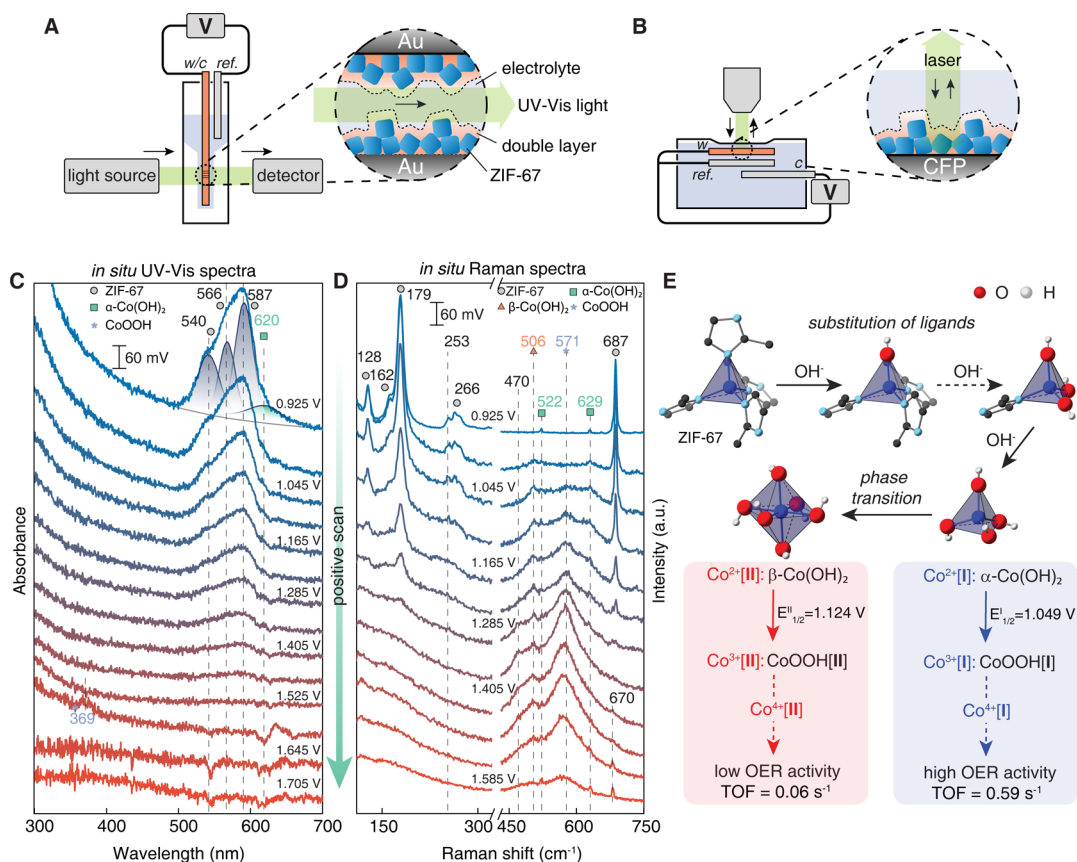


Figure 4. In situ spectroelectrochemical studies of ZIF-67 and proposed structural evolution. Simplified cell configuration and sampling of the electrode surface during (A) in situ UV-vis experiment and (B) in situ Raman experiment. w = working electrode, c = counter electrode, and ref. = reference electrode. (C) In situ UV-vis spectroelectrochemical study between 0.925 and 1.705 V. (D) In situ Raman spectroelectrochemical study between 0.925 and 1.585 V. Only forward scans are shown. The sampling interval is 60 mV. (E) Illustration of the precatalytic conversion of ZIF-67 to α -Co(OH)₂ and β -Co(OH)₂ and their further oxidation and OER activity.

cycle. The in situ electrochemical cells of both techniques and the integrated polarization curves are shown in Figure S7A,B. To clarify, the simplified cell configurations and sampling processes during the in situ spectroelectrochemistry are shown in Figure 4A,B. For in situ UV-vis spectroscopy, a transmission configuration was used, in which the UV-vis light travels through the Au-coated tunnels of the working electrode (Au honeycomb electrode) to reach the detector. During the experiment, the tunnels are coated with a layer of ZIF-67 particles. As a result, the UV-vis light can collect structural information by interacting with the species on the surface of the electrode and in the double layer. The in situ Raman experiment, on the other hand, adopts a similar configuration to the one for ex situ Raman tests except for an in situ cell to perform electrochemistry. The structural information of the bulk ZIF-67 and its surface species are collected during the electrochemical experiments.

Figure 4C shows the UV-vis spectra of ZIF-67 at various applied potentials. At 0.925 V, in addition to the uprising absorption <400 nm caused by the mIM linker, the broad absorption signal is obvious from 500 to 650 nm, which can be resolved to four peaks using Gaussian functions.³² The three main peaks at 540, 566, and 587 nm are known as the spin-orbital coupling triplet peaks, which can be assigned to the ${}^4A_2(F)$ to ${}^4T_1(P)$ transition of tetrahedral Co sites.³³ The absence of any peaks at 480 and 506 nm rules out the existence of any octahedral Co coordination in ZIF-67.³⁴ The minor

peak at 620 nm matches the adsorption edge of α -Co(OH)₂, which also features a tetrahedral Co coordination.³⁵ The formation of α -Co(OH)₂ could be attributed to the coordination of surface Co with H₂O during synthesis. In the positive scan from 0.925 to 1.705 V, the intensity of the triplet peaks gradually decreases until vanishes at 1.525 V, and the peak at 620 nm persists until 1.465 V. The decrement indicates the destruction of surface tetrahedral coordination environment in ZIF-67, and the decreased absorption <400 nm also confirms the loss of mIM linkers. As demonstrated by previous electrochemical and ex situ characterization results, the MOF structure sequentially undergoes $\text{Co}^{2+} \rightarrow \text{Co}^{3+} \rightarrow \text{Co}^{4+}$ electrooxidation and oxygen evolution with increasing potential. Therefore, the destruction could be attributed to the potential-driven formation of Co-OH⁻ coordination and/or Co^{2+} to Co^{3+} electrooxidation. Notably, as the potential rises from 1.525 to 1.585 V, a zigzag signal evolves at around 630 nm, which can be resolved to at least two overlapping peaks (one decreasing while the other increasing). On the one hand, the decreasing signal agrees with the peak of α -Co(OH)₂ at 620 nm, thereby representing the rapid consumption of α -Co(OH)₂. On the other hand, the increasing peak can be related to the CoOOH produced via electrooxidation. The generation of Co^{3+} species is also confirmed by an intense signal at 369 nm appearing at 1.585 V.³⁴ It is thus convincing that the produced Co^{3+} species is originated from α -Co(OH)₂, indicating that the previously identified $\text{Co}^{2+}[\text{I}]$ species is most

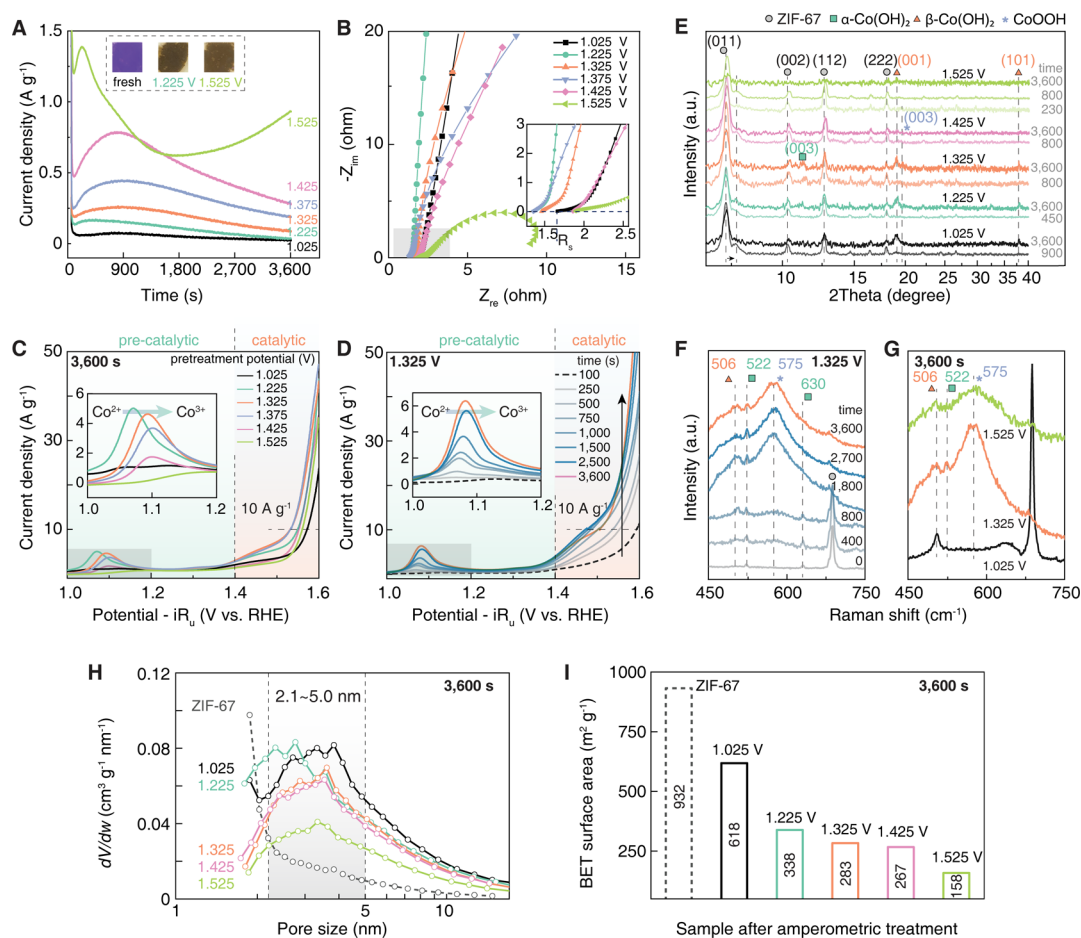


Figure 5. Amperometric treatment of ZIF-67@CFP electrode and the electrochemical properties of treated samples and structural characterization. (A) Amperometric plots of the ZIF-67@CFP electrode at selected applied potentials in 1.0 M KOH electrolyte. Insets are the digital images of the electrode surface before and after treatments (colorless indium tin oxide electrodes are used for photo taking). (B) Nyquist plots and (C) polarization curves of the ZIF-67@CFP electrode after amperometric treatment at selected applied potentials for 1 h. (D) Polarization curves of the ZIF@CFP electrode obtained after amperometric treatment at 1.325 V after different durations. (E) XRD patterns of ZIF-67 after amperometric treatment at various potentials and time. (F) In situ Raman spectra of ZIF-67 at different durations during the amperometric treatment at 1.325 V. (G) In situ Raman spectra of ZIF-67 after 1 h of amperometric treatment at 1.025, 1.325, and 1.525 V. (H) Pore size distribution plots and (I) BET surface area of pristine ZIF-67 and ZIF-67 samples treated by amperometry at different potentials for 1 h.

likely α -Co(OH)₂. However, it should be noted that the Co³⁺ production occurs at a much lower potential (ca. 1.04 V, Figure 2B). The absence of Co³⁺ signal below 1.585 V (but above the $E_{\text{Co}^{2+}/\text{Co}^{3+}}$) is most likely due to the relatively low concentration of Co³⁺, which accumulates and becomes detectable from 1.585 V.

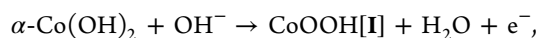
At higher potentials (1.645 and 1.705 V), the Co³⁺ signal disappears because of the subsequent Co³⁺ electrooxidation to Co⁴⁺. Furthermore, a reverse scan (Figure S7C) does not make the Co³⁺ disappear nor revive the trait peaks of ZIF-67, indicating the irreversible structural destruction of ZIF-67. No significant β -Co(OH)₂ signal is found, possibly because of its minor signal compared to the noise contributed by the produced O₂ bubbles at high potential.

The in situ Raman spectroelectrochemistry provides more sensitive real-time insights into the structural evolution process. A low laser power (1.5 mW) is applied to avoid phase transitions from CoOOH to Co₃O₄ triggered by laser heating.³⁶ The region between 100 and 750 cm⁻¹ reflecting the lattice vibrations is shown in Figure 4D. The characteristic Raman peaks of ZIF-67 at 162 and 179 cm⁻¹ are attributed to the nitrogen–cobalt–nitrogen (N–Co–N) deformation vi-

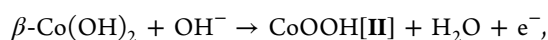
bration modes³⁷ and the peaks at 266 and 687 cm⁻¹ to the C–CH₃ stretching of mIM linker molecules.³⁸ At 0.925 V, the minor peak at 629 cm⁻¹ is assigned to the E_g vibration mode of α -Co(OH)₂, while the absence of A_{2u} mode (ca. 501 cm⁻¹) implies no β -Co(OH)₂.³⁹ The peak at 522 cm⁻¹ matches with the previous report of α -Co(OH)₂, and the shoulder peak at 253 cm⁻¹ suggests the four-coordinated Co sites from α -Co(OH)₂.⁴⁰ Such peaks indicate the formation of α -Co(OH)₂ after immersing ZIF-67 into the electrolyte. As the applied potential rises from 0.925 to 0.985 V, a new peak develops at 506 cm⁻¹, close to the A_{2u} vibration peak of β -Co(OH)₂, declaring its formation. At 1.045 V, the electrooxidation of Co²⁺ to CoOOH starts, and the low crystallinity of CoOOH is suggested by its broad A_{1g} peak at ca. 571 cm⁻¹. This lack of local crystallinity makes it impossible to differentiate the CoOOH species produced by α - and β -Co(OH)₂. Interestingly, the traits of ZIF-67 remain without significant loss of peak intensity, which implies the formation of α/β -Co(OH)₂, and their corresponding CoOOH forms are mainly limited on the surface of ZIF-67. Increasing the potential to 1.225 V leads to the rapid decline of ZIF-67 peaks and the rise of CoOOH A_{1g} peak at 571 cm⁻¹, while the broad peaks between 450 and

650 cm^{-1} reveal the extensive formation of $\text{Co}(\text{OH})_2$ (both α and β phase). No ZIF-67 structure is detected by Raman scattering above 1.285 V, and the dominating peak at 571 cm^{-1} indicates the conversion of most Co species to CoOOH . Meanwhile, minor peaks (470 and 670 cm^{-1} at 1.285 and 1.525 V, respectively) are observed, matching the E_g and A_{1g} modes of Co_3O_4 .⁴¹ However, as no Co_3O_4 structure is observed by XRD nor XPS, it is likely due to the phase transition of $\text{CoOOH}/\text{Co}(\text{OH})_2$ to Co_3O_4 by laser heating (a higher laser power of 5.0 mW leads to full conversion to Co_3O_4 as shown in Figure S8).⁴² The reverse scan (Figure S7D) shows the incomplete reduction of CoOOH to $\text{Co}(\text{OH})_2$ as indicated by the intense A_{2u} peak at 504 cm^{-1} , which echoes the CV results that the Co^{3+} species are not sufficiently reduced and less active Co^{2+} species ($\beta\text{-Co}(\text{OH})_2$) is produced. It is thus clear that the previously mentioned $\text{Co}^{2+}[\text{I}]$ and $\text{Co}^{2+}[\text{II}]$ are α - and β - $\text{Co}(\text{OH})_2$, respectively.

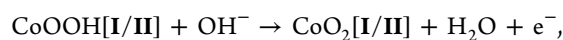
Based on the in situ and ex situ studies, the evolution of the Co sites in ZIF-67 during CV precatalytic treatments is proposed as follows



$$E = E_{\text{Co}^{2+}/\text{Co}^{3+}}^{\text{I}}$$



$$E = E_{\text{Co}^{2+}/\text{Co}^{3+}}^{\text{II}}$$



$$E = E_{\text{Co}^{3+}/\text{Co}^{4+}}^{\text{I/II}}$$

After exposing ZIF-67 to the alkaline electrolyte (Figure 4E), the hydroxide ions would replace the mIM molecules of the tetrahedral Co sites on the surface layer of ZIF-67 to form $\text{Co}(\text{mIM})_3\text{OH}$, $\text{Co}(\text{mIM})_2(\text{OH})_2$, $\text{Co}(\text{mIM})(\text{OH})_3^-$, and eventual $\text{Co}(\text{OH})_4^{2-}$ ($\alpha\text{-Co}(\text{OH})_2$). As a result of CV treatment, the capacitive adsorption of OH^- further assists such replacements to the inner layers. Meanwhile, the phase transition from $\alpha\text{-Co}(\text{OH})_2$ to $\beta\text{-Co}(\text{OH})_2$ occurs.⁴³ During Co^{2+} to Co^{3+} electrooxidation, both α - and $\beta\text{-Co}(\text{OH})_2$ (assigned to previous $\text{Co}^{2+}[\text{I}]$ and $\text{Co}^{2+}[\text{II}]$ species) are converted to their corresponding CoOOH (denoted as $\text{CoOOH}[\text{I}]$ and $\text{CoOOH}[\text{II}]$). Despite its instability, the α phase sites are 9.8 times more active ($\text{TOF} = 0.59 \text{ s}^{-1}$) compared to the β phase sites ($\text{TOF} = 0.06 \text{ s}^{-1}$).

Regarding the structure of $\text{CoOOH}[\text{I}]$ and $\text{CoOOH}[\text{II}]$, it is worth emphasizing that a few reports suggested that the electrooxidation products of $\alpha\text{-Co}(\text{OH})_2$ and $\beta\text{-Co}(\text{OH})_2$ are $\gamma\text{-CoOOH}$ and $\beta\text{-CoOOH}$, respectively, which is yet to be verified by others.^{27,44} Moreover, the assignment of $\text{CoOOH}[\text{I}]$ and $\text{CoOOH}[\text{II}]$ cannot be done based on our spectral evidence because of the poor signal-to-noise ratio of in situ experiment and the overlapping signals from $\text{Co}(\text{OH})_2$ and ZIF-67. Therefore, it is reasonable for us to only show the existence of two types of CoOOH here without discussing their detailed structure.

2.5. Amperometric Treatment of ZIF-67. The amperometric study is another standard electrochemical method often used to evaluate the electrocatalytic stability of materials at a certain potential. Similar to CV, the amperometric treatment

also involves multiple processes driven by the applied potential. In amperometry, however, a fixed potential is applied while the current signal is recorded. At a given potential, amperometry allows us to accumulate redox products while monitoring the electron exchange rate.

Figure 5A shows the amperometric plots of ZIF-67. With applied potentials lower than 1.525 V, the current rises until ca. 800 s after the initial drop of non-Faradaic current (charging current) within ca. 10 s and declines between 800 and 3600 s. At 1.025 V, the current increment from 0.060 to 0.078 A g^{-1} at 900 s indicates the slightly enlarged ECSA, possibly because of the mass transfer of OH^- into the pores of ZIF-67 because no Faradaic current is expected. Meanwhile, the replacement of mIM linkers by OH^- converts ZIF-67 to α - and $\beta\text{-Co}(\text{OH})_2$, which have a poorer porosity than ZIF-67, explaining the current decline to 0.023 A g^{-1} after 3600 s. Once the onset potential of Co^{2+} electrooxidation is reached (i.e., $E \geq 1.325 \text{ V}$), the Faradaic current dominates as a higher potential showing a higher kinetic rate. Because the current is controlled by the concentration gradient of accessible Co^{2+} and OH^- , the diffusion of OH^- and the formation of $\text{Co}(\text{OH})_2$ benefit the accessible Co^{2+} concentration, leading to the current increase until 800 s. After reaching the highest gradient, the produced CoOOH dominates the surface, surpassing Co^{2+} species and causing the current to decline. Further increase of potential to 1.525 V leads to $\text{Co}^{2+}\text{-Co}^{3+}\text{-Co}^{4+}$ electrooxidation. The clear indication of OER current boost is evident from 1800 s, and the previous $\text{Co}^{2+}\text{-Co}^{3+}\text{-Co}^{4+}$ process can be regarded as the "activation" process because both Co^{3+} and Co^{4+} are regarded as the real active sites.²⁰

After the amperometric treatment for 1 h, the samples demonstrate diverse ion transport rates and OER activities as shown by the Nyquist plots and polarization curves (Figure 5B,C). Below 1.425 V, all electrodes show excellent ion transports as indicated by the phase angles larger than 45° . The amperometric treatment at 1.525 V renders a depressed semicircular arc, an indication of a single-step charge-transfer reaction (Co^{3+} to Co^{4+} electrooxidation), yet the smaller phase angle of samples treated at 1.525 V for 1 h indicates the decreased ECSA. Meanwhile, the noncompensated resistance (R_s) obtained from the high-frequency region (inset of Figure 5B) reveals the conductivity of the modified electrode because the electrolyte resistance is the same for all. The difference in R_s is determined by the conductivity of the electrocatalyst layer as well as the contact resistance between the CFP and the electrocatalyst.⁴⁵ The sample treated at 1.225–1.375 V shows a lower resistance of ca. 1.4 Ω compared to 1.6 Ω (1.025 V) and 1.9 Ω (1.425 and 1.525 V) of the others. The most reasonable explanation is that the formation of CoOOH can reduce the noncompensated resistance, while the production of Co^{4+} species either decreases the conductivity or undermines the contact of the electrode/catalyst interface.

Depending on the pretreatment potential, a significantly different OER performance is achieved. As indicated by the inset of Figure 5C, after iR compensation, the precatalytic treatment at 1.025 V produces minor accessible Co^{2+} species, while those at 1.225, 1.325, and 1.375 V result in the dramatically increased Co^{2+} populations ($\text{Co}(\text{OH})_2$). The peak shifting of $\text{Co}^{2+}\text{-Co}^{3+}$ oxidation potential after pretreatment at 1.225 and 1.325 V suggests the involvement of more than one Co^{2+} species (suggested below by in situ Raman spectra as $\alpha/\beta\text{-Co}(\text{OH})_2$ in Figure 5G, Section 2.6) and their potential-dependent content.

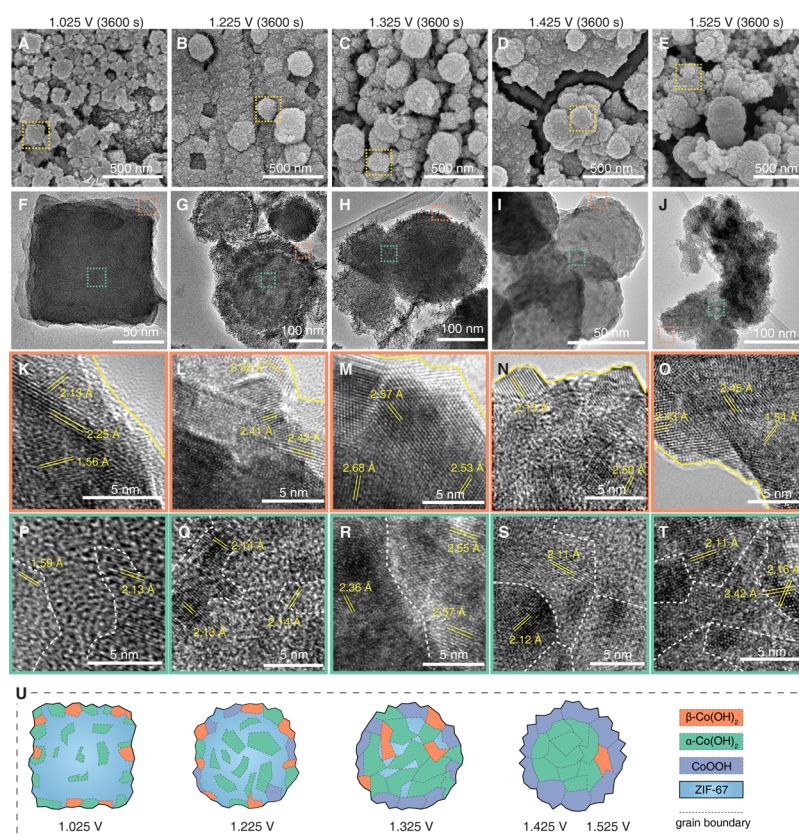


Figure 6. Morphology of ZIF-67@CFP electrode after amperometric study. (A–E) SEM and (F–J) TEM images of ZIF-67 after amperometric treatment at various applied potentials for 1 h. (K–T) TEM images of the (K–O) edge (marked in red) and (P–T) center (marked in blue) regions of the corresponding TEM image. The lattice spacings and grain boundaries are illustrated in yellow and dotted lines, respectively. (U) Illustration of the structural evolution of electrocatalyst after amperometric study at the different potential values.

Higher pretreatment potential (>1.325 V) leads to major Co^{2+} to Co^{3+} oxidation before the polarization tests, leaving a smaller amount of Co^{2+} to form the oxidation peak during the precatalytic region of OER polarization curve. Figure 5C shows that the subsequent OER overpotential at 10 A g^{-1} decreases from 341 mV (pretreated at 1.025 V) to 300 mV (pretreated at 1.325 V) with Tafel slope (Figure S9) increasing from 78.6 to 99.4 mV dec^{-1} . The trend of Tafel slope indicates, despite low total numbers, that the Co^{2+} sites produced by amperometric treatment at 1.025 V (most likely tetrahedral $\alpha\text{-Co(OH)}_2$ sites) have the highest activity toward OER after precatalytic activation. After treatment at a higher potential of 1.325 V, the large population of Co^{2+} sites ($\beta\text{-Co(OH)}_2$ sites) compensates the lower activity of the individual site. As the pretreatment potential rises to 1.425 and 1.525 V, most Co^{2+} sites have been already oxidized to their Co^{3+} form (CoOOH), showing higher site activity as indicated by the low Tafel slope of 70 mV dec^{-1} (Figure S9), however, as well as higher overpotential (330 mV) because of the decreased total site numbers suggested by the smaller ECSA (Figure SB).

To refine the correlation between amperometric treatment and OER activity, the OER tests are performed using the ZIF-67@CFP electrode pretreated at 1.325 V for different durations (Figure 5D). From 100 to 3600 s, as shown in the precatalytic region, more Co^{2+} sites are exposed for the electrooxidation to Co^{3+} . However, the TOF (overpotential = 300 mV) maintains at ca. 0.24 s^{-1} with pretreatment time between 100 and 1000 s but drops to 0.13 and 0.043 s^{-1} after pretreatment for 1500 and 3600 s, respectively. Therefore,

despite the increased site number, the single-site activity of Co drops by 82%. The joint influence of OER performance by the two counterparts is well reflected by the volcano-shaped overpotential trend, which decreases from 362 mV (100 s) to 239 mV (2500 s) and rises to 293 mV (3600 s). The reasonable explanation is that, at a short duration (100–1000 s), only a small amount of high active Co sites are produced (identified as $\alpha\text{-Co(OH)}_2$ in Figure 5F, Section 2.6), leading to high TOF yet high overpotential because of the limited number. Prolonged durations, in contrast, produce sufficient sites but mainly in the low active form ($\beta\text{-Co(OH)}_2$). Only optimal duration (1000–2500 s) can offer an acceptable site population while maintaining mainly the $\alpha\text{-Co(OH)}_2$ form.

2.6. Structural and Morphological Evolution of ZIF-67 during Amperometry. XRD and in situ Raman spectroscopy are engaged to verify the structure degradation of ZIF-67 during amperometric pretreatment. XRD plots in Figure 5E reveal the deformation of ZIF-67 suggested by the shoulder peak at 7.7° besides its (011) peak. Below 1.425 V, the coexistence of $\beta\text{-Co(OH)}_2$ and ZIF-67 is widely observed, along with the minor peak of CoOOH (003) plane if treated between 1.225 and 1.425 V. After OER occurs at 1.525 V, only the peak of ZIF-67 (011) plane is observed with a small indication of (001) peak from $\beta\text{-Co(OH)}_2$. The broadening of $\beta\text{-Co(OH)}_2$ peak and disappearance of CoOOH peak at 1.525 V are due to the decreased crystallite size beyond the XRD detection limit. Most interestingly, when treated at 1.325 V, the diffraction peak at 11.7° corresponding to the (003) facet of $\alpha\text{-Co(OH)}_2$ arises,⁴³ while no $\beta\text{-Co(OH)}_2$ peaks are

observed at 800 s. β -Co(OH)₂ only appears at a longer time of 3600 s. In conjunction with Figure 5D, it is clear that Co³⁺ species produced from α -Co(OH)₂ is more active than Co³⁺ species from β -Co(OH)₂. The findings from in situ Raman spectra (Figure 5F) also support this argument because the vibration bands at 522 and 630 cm⁻² are exclusively assigned to α -Co(OH)₂. Figure 5G compares the spectra obtained after 1 h treatment at 1.025 V (only capacitive behavior), 1.325 V (electrooxidation of Co²⁺ to Co³⁺), and 1.525 V (dominated by OER), showing that only the treatment at 1.325 V leads to the detectable production of α -Co(OH)₂.

Figure 5H,I compares the pore size distribution and Brunauer–Emmett–Teller (BET) surface area of pristine ZIF-67 and ZIF-67 samples treated by amperometry at different potentials for 1 h. The sub-2 nm pore observed from the pristine sample matches well with the theoretical 1.7 nm pore (Figure 1A). After amperometric treatments at 1.025 and 1.225 V, the population of the sub-2 nm pores drops rapidly, while new pore structure(s) with diameters of 2.1–5.0 nm forms, which echoes the destruction of ZIF-67 structure and the formation of porous α -/ β -Co(OH)₂. Further increased amperometric potentials (1.325 and 1.425 V) lead to minor sub-2 nm pores and dominating larger pores between 2.1 and 5.0 nm, marking the established α -/ β -Co(OH)₂ structure. As the potential reaches 1.525 V, the population of the pores with diameters of 2.1–5.0 nm drops, possibly caused by further electrooxidation of α -/ β -Co(OH)₂ structure. Meanwhile, the BET surface area of ZIF-67 declines dramatically during amperometry, from 932 to 158 m² g⁻¹ after 1 h treatment at 1.525 V.

Figure 6 shows the morphological evolution of ZIF-67 (zoom-out images shown in Figure S10). Again, no observable electron damage is evident during the imaging process. Despite the interference from lattice disorder, the interplanar spacing (*d* spacing) can provide insights toward the formed structures. At 1.025 V, polycrystalline structures appear on both edge and bulk regions of deformed ZIF-67 nanocubes. The *d* spacings of ca. 1.59 and 2.13 Å can be ascribed to the (110) and (018) planes of α -Co(OH)₂, respectively.⁴⁶ The presence of β -Co(OH)₂ is also suggested by the *d* spacing of 2.25 Å, matching the (101) plane. Therefore, both α and β phases of Co(OH)₂ coexist on the surface of the deformed ZIF-67, while the α phase dominates the bulk material, decorated in the ZIF-67 matrix. The α -to- β phase transition only occurs on the surface region because only the surface α -Co(OH)₂ is in direct contact with sufficient hydroxide ions, which is essential for a phase transition.⁴⁰ At a higher treatment potential of 1.225 V, no cubic particles are evident. Instead, aggregated spherical particles are formed and the cubic vacancies left by the detached ZIF-67 particles are visible. Clear grain boundaries with *d* spacings of ca. 2.43 and 2.32 Å are shown in the edge region, which are attributed to the (101) plane of CoOOH and the (101) plane of β -Co(OH)₂, respectively, suggesting the surface covered by CoOOH and Co(OH)₂. However, the center region only shows the *d* spacing of 2.14 Å, indicating the extensive presence of α -Co(OH)₂. The higher amperometric potential at 1.325 V leads to the wide formation of a well-defined α -Co(OH)₂ nanocrystal with a *d* spacing of ca. 2.68 Å ((100) plane)⁴⁷ on the surface as well as CoOOH (possibly α phase with the *d* spacing of 2.57 Å). Further raising the potential to 1.425 and 1.525 V results in the spherical nanoparticles with cracks and pores. At 1.525 V, polycrystalline structures are observed with mainly CoOOH on the surface (*d*

spacing of 2.43 Å ascribed to (101) plane),⁴⁸ while the bulk particles still show the presence of α -Co(OH)₂.

3. CONCLUSIONS

In summary, ZIF-67, as a widely employed example of the MOFs in recent electrochemical applications, is unstable during two common electrochemical studies: CV and amperometry. The real active sites for OER are the intermediates generated by electrochemistry, not the metal nodes.

CV treatment brings a dramatic and irreversible morphological change to ZIF-67 from cube to the irregular sphere within merely 15 cycles. Even within the potential window lower than the redox potential (at $E < E_{\text{Co}^{2+}/\text{Co}^{3+}}$), the sweeping potential sabotages the tetrahedral Co²⁺–organic linker coordination and reveals the electron-accessible Co²⁺ species with increasing cycle number. In situ UV–vis and Raman spectra of the first cycle, as well as ex situ characterizations (XRD and XPS), suggest the rapid replacement of the coordinated organic linkers by OH⁻, forming tetrahedral α -Co(OH)₂, followed by the phase transition to its octahedral β phase. At the higher potential during the forward scan (at $E > E_{\text{Co}^{2+}/\text{Co}^{3+}}$), the exposed Co²⁺ sites are further oxidized to their high-valent forms (γ -CoOOH and β -CoOOH), acting as the real active sites for OER, demonstrating the OER TOF of 0.59 and 0.06 s⁻¹ at an overpotential of 296 mV, respectively. The reverse scan can partially reduce CoOOH to Co(OH)₂ but cannot restore the Co²⁺–organic linker coordination.

Amperometric treatment at selected applied potentials also reveals the electrochemical instability of ZIF-67. Rapid morphological and structural changes happen within 900 s, producing mainly α -Co(OH)₂ in the bulk and polycrystalline structure of α -/ β -Co(OH)₂ as well as CoOOH (at $E > E_{\text{Co}^{2+}/\text{Co}^{3+}}$) on the surface. Higher potential and longer amperometric treatments result in more Co²⁺ exposure but also the conversion of α -Co(OH)₂ to its less active β phase. Consequently, the in situ-produced hybrid α -/ β -Co(OH)₂ species (and their oxidized forms of Co³⁺ and Co⁴⁺) on the surface of ZIF-67 during the electrochemical test are the dominating active sites for OER, other than the unstable Co nodes of ZIF-67. The overall performance (overpotential) is controlled by the total number of Co sites and the relative contents of CoOOH produced by α -/ β -Co(OH)₂.

On the comprehensive demonstration of the electrochemical instability of ZIF-67, we have confirmed that both CV and amperometric characterizations are destructive methods for MOFs study. In alkaline electrolyte, the sweeping potential during CV can result in a relatively fast destruction of ZIF-67 and the formation of Co(OH)₂/CoOOH because of the dynamical electrochemical double layer driven by potential. Differently, the fixed potential during amperometry forms a relatively stable double-layer structure, in which the replacement of coordinated organic linkers by OH⁻ occurs from surface to bulk MOF, as well as the electrooxidation from Co(OH)₂ to CoOOH.

Therefore, the information acquired from electrochemical methods may not provide genuine insights toward the real properties of MOFs, other than the intermediates produced chemically and electrochemically. Similarly, the catalytic findings from electrochemistry cannot be attributed to MOFs automatically without careful study of the actual journey of the MOFs. In future MOF studies, especially those that directly use MOFs as electrocatalysts, it is needed to examine the

structure during and after electrochemical and electrocatalytic studies to ensure the role of MOFs and guide appropriate electrocatalyst design.

■ ASSOCIATED CONTENT

Supporting Information

The Supporting Information is available free of charge at <https://pubs.acs.org/doi/10.1021/acscatal.9b03790>.

Synthesis of ZIF-67, characterization methods, electrochemical characterization details, TOF calculation, Nyquist plots, examples of CV curve fitting, Tafel plots, XPS spectra, SEM images, in situ spectroelectrochemical experimental setup and the reverse scan, and laser intensity study (PDF)

Continuous imaging of edge of ZIF-67 (MP4)

■ AUTHOR INFORMATION

Corresponding Author

*E-mail: lawrence.ys.lee@polyu.edu.hk

ORCID

Weiran Zheng: 0000-0002-9915-6982

Lawrence Yoon Suk Lee: 0000-0002-6119-4780

Author Contributions

W.Z. and M.L. contributed equally to this work. W.Z. designed the experiments, conducted the electrochemical experiments (CV, EIS, and in situ UV-vis SPECE), as well as data analysis and visualization. M.L. performed the in situ Raman SPECE, XRD, XPS, FESEM, and TEM. L.Y.S.L. supervised the progress of this project and drafted the manuscript with W.Z.

Notes

The authors declare no competing financial interest.

■ ACKNOWLEDGMENTS

This work was supported by the Innovation and Technology Commission of Hong Kong and the Hong Kong Polytechnic University (grant number 1-BE0Y).

■ REFERENCES

- (1) Stock, N.; Biswas, S. Synthesis of Metal-Organic Frameworks (MOFs): Routes to Various MOF Topologies, Morphologies, and Composites. *Chem. Rev.* **2012**, *112*, 933–969.
- (2) Eddaoudi, M.; Kim, J.; Rosi, N.; Vodak, D.; Wachter, J.; O’Keeffe, M.; Yaghi, O. M. Systematic Design of Pore Size and Functionality in Isoreticular MOFs and Their Application in Methane Storage. *Science* **2002**, *295*, 469–472.
- (3) Morozan, A.; Jaouen, F. Metal Organic Frameworks for Electrochemical Applications. *Energy Environ. Sci.* **2012**, *5*, 9269–9290.
- (4) Downes, C. A.; Marinescu, S. C. Electrocatalytic Metal-Organic Frameworks for Energy Applications. *ChemSusChem* **2017**, *10*, 4374–4392.
- (5) Zheng, W.; Tsang, C.-S.; Lee, L. Y. S.; Wong, K.-Y. Two-Dimensional Metal-Organic Framework and Covalent-Organic Framework: Synthesis and Their Energy-Related Applications. *Mater. Today Chem.* **2019**, *12*, 34–60.
- (6) Xu, Y.; Li, Q.; Xue, H.; Pang, H. Metal-Organic Frameworks for Direct Electrochemical Applications. *Coord. Chem. Rev.* **2018**, *376*, 292–318.
- (7) Zhu, C.; Fu, S.; Shi, Q.; Du, D.; Lin, Y. Single-Atom Electrocatalysts. *Angew. Chem., Int. Ed.* **2017**, *56*, 13944–13960.
- (8) Qin, J.-S.; Du, D.-Y.; Guan, W.; Bo, X.-J.; Li, Y.-F.; Guo, L.-P.; Su, Z.-M.; Wang, Y.-Y.; Lan, Y.-Q.; Zhou, H.-C. Ultrastable Polymolybdate-Based Metal-Organic Frameworks as Highly Active

Electrocatalysts for Hydrogen Generation from Water. *J. Am. Chem. Soc.* **2015**, *137*, 7169–7177.

(9) Flügel, E. A.; Lau, V. W.-h.; Schlögl, H.; Glaum, R.; Lotsch, B. V. Homonuclear Mixed-Valent Cobalt Imidazolate Framework for Oxygen-Evolution Electrocatalysis. *Chem.—Eur. J.* **2016**, *22*, 3676–3680.

(10) Ghoshal, S.; Zaccarine, S.; Anderson, G. C.; Martinez, M. B.; Hurst, K. E.; Pylypenko, S.; Pivovar, B. S.; Alia, S. M. ZIF 67 Based Highly Active Electrocatalysts as Oxygen Electrodes in Water Electrolyzer. *ACS Appl. Energy Mater.* **2019**, *2*, 5568–5576.

(11) Zhao, S.; Wang, Y.; Dong, J.; He, C.-T.; Yin, H.; An, P.; Zhao, K.; Zhang, X.; Gao, C.; Zhang, L.; Lv, J.; Wang, J.; Zhang, J.; Khattak, A. M.; Khan, N. A.; Wei, Z.; Zhang, J.; Liu, S.; Zhao, H.; Tang, Z. Ultrathin Metal-Organic Framework Nanosheets for Electrocatalytic Oxygen Evolution. *Nat. Energy* **2016**, *1*, 16184.

(12) Zhou, W.; Huang, D.-D.; Wu, Y.-P.; Zhao, J.; Wu, T.; Zhang, J.; Li, D.-S.; Sun, C.; Feng, P.; Bu, X. Stable Hierarchical Bimetal-Organic Nanostructures as High Performance Electrocatalysts for the Oxygen Evolution Reaction. *Angew. Chem., Int. Ed.* **2019**, *58*, 4227–4231.

(13) Liu, M.; Zheng, W.; Ran, S.; Boles, S. T.; Lee, L. Y. S. Overall Water-Splitting Electrocatalysts Based on 2D CoNi-Metal-Organic Frameworks and Its Derivative. *Adv. Mater. Interfaces* **2018**, *5*, 1800849–1800857.

(14) Shen, J.-Q.; Liao, P.-Q.; Zhou, D.-D.; He, C.-T.; Wu, J.-X.; Zhang, W.-X.; Zhang, J.-P.; Chen, X.-M. Modular and Stepwise Synthesis of a Hybrid Metal-Organic Framework for Efficient Electrocatalytic Oxygen Evolution. *J. Am. Chem. Soc.* **2017**, *139*, 1778–1781.

(15) Wang, X.-L.; Dong, L.-Z.; Qiao, M.; Tang, Y.-J.; Liu, J.; Li, Y.; Li, S.-L.; Su, J.-X.; Lan, Y.-Q. Exploring the Performance Improvement of the Oxygen Evolution Reaction in a Stable Bimetal-Organic Framework System. *Angew. Chem., Int. Ed.* **2018**, *57*, 9660–9664.

(16) Cheng, W.; Zhao, X.; Su, H.; Tang, F.; Che, W.; Zhang, H.; Liu, Q. Lattice-Strained Metal-Organic-Framework Arrays for Bifunctional Oxygen Electrocatalysis. *Nat. Energy* **2019**, *4*, 115–122.

(17) Rui, K.; Zhao, G.; Chen, Y.; Lin, Y.; Zhou, Q.; Chen, J.; Zhu, J.; Sun, W.; Huang, W.; Dou, S. X. Hybrid 2D Dual-Metal-Organic Frameworks for Enhanced Water Oxidation Catalysis. *Adv. Funct. Mater.* **2018**, *28*, 1801554–1801563.

(18) Chen, Z.; Cai, L.; Yang, X.; Kronawitter, C.; Guo, L.; Shen, S.; Koel, B. E. Reversible Structural Evolution of NiCoO_xH_y During the Oxygen Evolution Reaction and Identification of the Catalytically Active Phase. *ACS Catal.* **2018**, *8*, 1238–1247.

(19) Brodsky, C. N.; Hadt, R. G.; Hayes, D.; Reinhart, B. J.; Li, N.; Chen, L. X.; Nocera, D. G. In Situ Characterization of Cofacial Co(IV) Centers in Co₄O₄ Cubane: Modeling the High-Valent Active Site in Oxygen-Evolving Catalysts. *Proc. Natl. Acad. Sci. U.S.A.* **2017**, *114*, 3855–3860.

(20) Favaro, M.; Yang, J.; Nappini, S.; Magnano, E.; Toma, F. M.; Crumlin, E. J.; Yano, J.; Sharp, I. D. Understanding the Oxygen Evolution Reaction Mechanism on CoO_x Using Operando Ambient-Pressure X-ray Photoelectron Spectroscopy. *J. Am. Chem. Soc.* **2017**, *139*, 8960–8970.

(21) Zhao, X.; Pattengale, B.; Fan, D.; Zou, Z.; Zhao, Y.; Du, J.; Huang, J.; Xu, C. Mixed-Node Metal-Organic Frameworks as Efficient Electrocatalysts for Oxygen Evolution Reaction. *ACS Energy Lett.* **2018**, *3*, 2520–2526.

(22) Hu, H.; Guan, B. Y.; Lou, X. W. Construction of Complex CoS Hollow Structures with Enhanced Electrochemical Properties for Hybrid Supercapacitors. *Chem* **2016**, *1*, 102–113.

(23) Zhang, D.; Zhu, Y.; Liu, L.; Ying, X.; Hsiung, C.-E.; Sougrat, R.; Li, K.; Han, Y. Atomic-Resolution Transmission Electron Microscopy of Electron Beam-Sensitive Crystalline Materials. *Science* **2018**, *359*, 675–679.

(24) Cho, S.; Chen, C.-F.; Mukherjee, P. P. Influence of Microstructure on Impedance Response in Intercalation Electrodes. *J. Electrochem. Soc.* **2015**, *162*, A1202–A1214.

- (25) Fan, K.; Zou, H.; Lu, Y.; Chen, H.; Li, F.; Liu, J.; Sun, L.; Tong, L.; Toney, M. F.; Sui, M.; Yu, J. Direct Observation of Structural Evolution of Metal Chalcogenide in Electrocatalytic Water Oxidation. *ACS Nano* **2018**, *12*, 12369–12379.
- (26) Zhou, K.; Mousavi, B.; Luo, Z.; Phatanasri, S.; Chaemchuen, S.; Verpoort, F. Characterization and Properties of Zn/Co Zeolitic Imidazolate Frameworks Vs. ZIF-8 and ZIF-67. *J. Mater. Chem. A* **2017**, *5*, 952–957.
- (27) Liu, Y.-C.; Koza, J. A.; Switzer, J. A. Conversion of Electrodeposited Co(OH)₂ to CoOOH and Co₃O₄, and Comparison of Their Catalytic Activity for the Oxygen Evolution Reaction. *Electrochim. Acta* **2014**, *140*, 359–365.
- (28) Qin, J.; Wang, S.; Wang, X. Visible-Light Reduction CO₂ with Dodecahedral Zeolitic Imidazolate Framework ZIF-67 as an Efficient Co-Catalyst. *Appl. Catal., B* **2017**, *209*, 476–482.
- (29) Casella, I. G.; Guascito, M. R. Anodic Electrodeposition of Conducting Cobalt Oxyhydroxide Films on a Gold Surface. XPS Study and Electrochemical Behaviour in Neutral and Alkaline Solution. *J. Electroanal. Chem.* **1999**, *476*, 54–63.
- (30) Yang, J.; Liu, H.; Martens, W. N.; Frost, R. L. Synthesis and Characterization of Cobalt Hydroxide, Cobalt Oxyhydroxide, and Cobalt Oxide Nanodiscs. *J. Phys. Chem. C* **2010**, *114*, 111–119.
- (31) Babar, P. T.; Lokhande, A. C.; Pawar, B. S.; Gang, M. G.; Jo, E.; Go, C.; Suryawanshi, M. P.; Pawar, S. M.; Kim, J. H. Electrocatalytic Performance Evaluation of Cobalt Hydroxide and Cobalt Oxide Thin Films for Oxygen Evolution Reaction. *Appl. Surf. Sci.* **2018**, *427*, 253–259.
- (32) Antonov, L.; Nedeltcheva, D. Resolution of Overlapping UV–Vis Absorption Bands and Quantitative Analysis. *Chem. Soc. Rev.* **2000**, *29*, 217–227.
- (33) Vrålstad, T.; Glomm, W. R.; Rønning, M.; Dathe, H.; Jentys, A.; Lercher, J. A.; Øye, G.; Stöcker, M.; Sjöblom, J. Spectroscopic Characterization of Cobalt-Containing Mesoporous Materials. *J. Phys. Chem. B* **2006**, *110*, 5386–5394.
- (34) El Haskouri, J.; Cabrera, S.; Gómez-García, C. J.; Guillem, C.; Latorre, J.; Beltrán, A.; Beltrán, D.; Marcos, M. D.; Amorós, P. High Cobalt Content Mesoporous Silicas. *Chem. Mater.* **2004**, *16*, 2805–2813.
- (35) Ma, R.; Liu, Z.; Takada, K.; Fukuda, K.; Ebina, Y.; Bando, Y.; Sasaki, T. Tetrahedral Co(II) Coordination in α -Type Cobalt Hydroxide: Rietveld Refinement and X-ray Absorption Spectroscopy. *Inorg. Chem.* **2006**, *45*, 3964–3969.
- (36) Pauporté, T.; Mendoza, L.; Cassir, M.; Bernard, M. C.; Chivot, J. Direct Low-Temperature Deposition of Crystallized CoOOH Films by Potentiostatic Electrolysis. *J. Electrochem. Soc.* **2005**, *152*, C49–C53.
- (37) Öztürk, Z.; Filez, M.; Weckhuysen, B. M. Decoding Nucleation and Growth of Zeolitic Imidazolate Framework Thin Films with Atomic Force Microscopy and Vibrational Spectroscopy. *Chem.—Eur. J.* **2017**, *23*, 10915–10924.
- (38) Carter, D. A.; Pemberton, J. E. Raman Spectroscopy and Vibrational Assignments of 1- and 2-Methylimidazole. *J. Raman Spectrosc.* **1997**, *28*, 939–946.
- (39) Koza, J. A.; Hull, C. M.; Liu, Y.-C.; Switzer, J. A. Deposition of β -Co(OH)₂ Films by Electrochemical Reduction of Tris-(Ethylenediamine)cobalt(III) in Alkaline Solution. *Chem. Mater.* **2013**, *25*, 1922–1926.
- (40) Rahbani, J.; Khashab, N. M.; Patra, D.; Al-Ghoul, M. Kinetics and Mechanism of Ionic Intercalation/De-Intercalation During the Formation of α -Cobalt Hydroxide and Its Polymorphic Transition to β -Cobalt Hydroxide: Reaction-Diffusion Framework. *J. Mater. Chem.* **2012**, *22*, 16361–16369.
- (41) Ludvigsson, M.; Lindgren, J.; Tegenfeldt, J. Incorporation and Characterisation of Oxides of Manganese, Cobalt and Lithium into Nafion 117 Membranes. *J. Mater. Chem.* **2001**, *11*, 1269–1276.
- (42) Usov, P. M.; McDonnell-Worth, C.; Zhou, F.; MacFarlane, D. R.; D'Alessandro, D. M. The Electrochemical Transformation of the Zeolitic Imidazolate Framework ZIF-67 in Aqueous Electrolytes. *Electrochim. Acta* **2015**, *153*, 433–438.
- (43) Kundu, S.; Malik, B.; Prabhakaran, A.; Pattanayak, D. K.; Pillai, V. K. Topotactic Transition of α -Co(OH)₂ to β -Co(OH)₂ Anchored on CoO Nanoparticles During Electrochemical Water Oxidation: Synergistic Electrocatalytic Effects. *Chem. Commun.* **2017**, *53*, 9809–9812.
- (44) Huang, J.; Liu, Q.; Yao, T.; Pan, Z.; Wei, S. XAFS Study on Structure-Activity Correlations of α -Co(OH)₂ Nanosheets Water Oxidation Catalysts. *J. Phys.: Conf. Ser.* **2016**, *712*, 012128.
- (45) Lasia, A. *Electrochemical Impedance Spectroscopy and Its Applications*; Springer, 2014.
- (46) Song, Z.; Han, X.; Deng, Y.; Zhao, N.; Hu, W.; Zhong, C. Clarifying the Controversial Catalytic Performance of Co(OH)₂ and Co₃O₄ for Oxygen Reduction/Evolution Reactions toward Efficient Zn-air Batteries. *ACS Appl. Mater. Interfaces* **2017**, *9*, 22694–22703.
- (47) Liu, P. F.; Yang, S.; Zheng, L. R.; Zhang, B.; Yang, H. G. Electrochemical Etching of α -Cobalt Hydroxide for Improvement of Oxygen Evolution Reaction. *J. Mater. Chem. A* **2016**, *4*, 9578–9584.
- (48) Huang, Y.; Zhao, X.; Tang, F.; Zheng, X.; Cheng, W.; Che, W.; Hu, F.; Jiang, Y.; Liu, Q.; Wei, S. Strongly Electrophilic Heteroatoms Confined in Atomic CoOOH Nanosheets Realizing Efficient Electrocatalytic Water Oxidation. *J. Mater. Chem. A* **2018**, *6*, 3202–3210.